PAPER

UV photodetector based on energy bandgap shifted hexagonal boron nitride nanosheets for high-temperature environments

IOP Publishing Journal of Physics D: Applied Physics
J. Phys. D: Appl. Phys. **51** (2018) 045102 (9pp) https://doi.org/10.1088/1361-6463/aa9fa8

UV photodetector based on energy bandgap shifted hexagonal boron nitride nanosheets for high-temperature environments

Manuel Rivera[1], **Rafael Velázquez**[1], **Ali Aldalbahi**[2], **Andrew F Zhou**[3] and **Peter X Feng**[1]

[1] Department of Physics, University of Puerto Rico, San Juan, PR 00936-8377, United States of America
[2] Department of Chemistry, College of Science, King Saud University, Riyadh 11451, Saudi Arabia
[3] Department of Physics, Indiana University of Pennsylvania, 975 Oakland Ave, Indiana, PA 15705, United States of America

E-mail: peter.feng@upr.edu

Received 12 September 2017, revised 5 December 2017
Accepted for publication 6 December 2017
Published 4 January 2018

Abstract

We extend our investigations in the use of boron nitride nanosheets (BNNSs) as sensing material for UV photodetectors by exploring the energy bandgap shift in a new BNNSs arrangement on silicon substrate produced by a pulsed laser plasma deposition (PLPD) technique. Characterizations by XRD and Raman spectrum analysis indicate that the material is composed of high purity hexagonal boron nitride (*h*BN). SEM and AFM images confirm this particular arrangement of BNNSs is made of randomly orientated *h*BN nanosheets. The BNNS on silicon substrate material exhibits higher conductivity and photosensitivity in deep UV region than previously investigated BNNS thin films. The material is also sensitive to the UVB region, indicative of having a lower band gap width than that of bulk or thin films, while remaining visible-blind. The observed decrease in cut-off frequency was a direct result of the structural arrangement of the BNNSs in the film. This has the advantage of avoiding doping in order to tune bandgap width, which can compromise intrinsic desirable properties of *h*BN. Additionally, the material performed extremely well as a UV photodetector even at temperatures as high as 400 °C, making this particular arrangement of BNNSs an ideal candidate for applications where UV sensing in high-temperature environments is required.

Keywords: UV photodetectors, boron nitride nanosheets, sensors

(Some figures may appear in colour only in the online journal)

1. Introduction

UV radiation can be categorized with respect to three distinct wavelength regions labeled as UVA, UVB and UVC, collectively spanning the entire UV spectrum (visible-blind). UVA covers the wavelengths from 400 to 315 nm, while UVB and UVC cover from 315 to 280 nm and from 280 to 100 nm, respectively [1]. The ability to detect UV radiation has a high value for a wide range of military, commercial and scientific applications [2–5]. For example, recent research has concluded that a decline of 1% in the volume of the ozone layer would cause an increase of 2% in UV radiation at ground level, resulting in an increase of 3% in the incident rate of skin cancer besides additional damages to exposed infrastructure and land crops [6–9]. Given the low threshold of human safe UV levels of exposure (3 mJ cm^{-2}) and the fact that most UV related damage is caused by UVB radiation, development of miniaturized, cost-effective and high precision devices capable of detecting both UVB and UVC radiation is presently highly regarded.

Solid-state UV 'visible-blind' detectors based on semiconductors have received particular attention due to the fact that they possess a band gap width corresponding to the UV region. Multiple wide band gap semiconductors such as diamond

[10, 11], nitride (AlN, GaN, BN) [12, 13], oxide (TiO_2, ZnO) and SiC [14–16] semiconducting materials have been investigated for their potential applications as sensing materials in deep UV photodetectors. A significant portion of the current research in this field is dedicated to the fabrication of UV detectors based on low-dimensional (LD) wide-bandgap inorganic semiconductor materials [17]. Such materials with tailored geometry have exhibited higher responsivity and photoconductivity gain than their conventional bulk and thin film counterparts because of their high surface area-to-volume ratios and the reduced dimension of the effective conductive channel [18–20].

Among the nitride semiconducting materials investigated, boron nitride (BN) has the advantage that it can be synthesized in different morphologies and nanoscale structures with relative ease, making it suitable for deep UV optoelectronic applications [21]. A variety of BN LD structures have been successfully synthesized including nanorods [22], nanotubes [23] and nanosheets (BNNSs) [24, 25]. Among these, BNNSs have received broad attention because they are the isoelectric analogs to the graphene structure and possess similar structural characteristics and physical properties [26]. BNNSs are composed of multi hexagonal boron nitride (*h*BN) monolayers stacked and held together by weak van der Waals forces. Recent studies have shown that BNNSs have a high potential for various applications, including uses in thermal conductivity, spintronics, tissue engineering, nanoscale supports for metal or metal oxide catalysts, deep ultraviolet light emitters, drug delivery platforms and labels, and critical components in nanodevices [27–29]. In addition, compared to traditional semiconducting materials, BNNSs possess superb thermal stability and chemical inertness, which renders it a desirable material for fabricating devices that can stand up to harsh environments.

High purity BNNSs usually have energy bandgap widths between 4.0 eV–5.5 eV, but major efforts have been successfully conducted towards developing BN energy bandgap width modulation techniques. As a result, BNNSs can now be synthesized with a wide range of energy bandgaps width even as low as 2 eV or less [30, 31]. This makes BNNSs an ideal candidate for application as visible-blind UV photodetectors, capable of having high selectivity within the UV spectral range combined with the previously mentioned benefits of BN such as endurance and chemical inertness. However, research on applications of BNNSs as the sensing component of UV sensors has not been as numerous as expected, mainly because obtaining high purity, defect-free BNNSs with minimal dislocations on the substrate has proven to be challenging. Moreover, most successful methods are capable of producing only small amounts of high-quality BNNSs [2, 32–34]. In the past, we have reported on a simple, fast and cost-effective technique based on pulsed laser plasma deposition (PLPD) capable of synthesizing large amounts of high-purity BNNSs over a wide range of substrates, as well as detailed structural analyses and UV detection performance tests of the obtained BNNSs [2, 32, 35, 36]. It was found that BNNSs were highly sensitive to deep UV light while exhibiting good repeatability and signal-to-noise ratio. In addition, it was observed in these reports that the thickness or number of stacked monolayers of *h*BN crystals in BNNSs had a significant impact on UV sensitivity and reaction times.

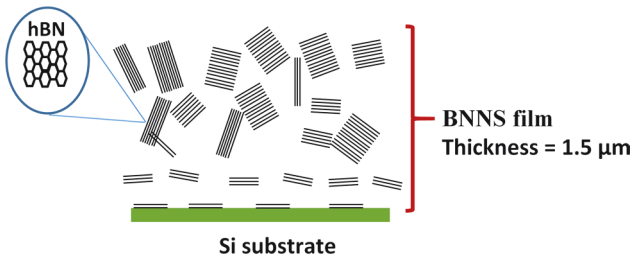

Figure 1. Illustration of BNNSs organization within thick BNNS film.

In this present work, we extend our investigations on the use of BNNSs as sensing material in UV photodetectors by exploring thick films composed of randomly orientated BNNSs on Si substrate applied to a metal-semiconductor-metal (MSM) photoconductor. An illustration of such an arrangement of BNNSs is depicted in figure 1. The UV detecting properties such as photocurrent, responsivity and cut-off frequency as well as their relationship to the BNNS film structure are discussed in detail.

2. Material and methods

2.1. Synthesis method

Pulsed CO_2 laser plasma beam deposition technique (PLPD) was used to synthesize our BNNS films. This deposition technique enables to reduce the films' stress and yield large, flat BNNSs. A detailed description of the applied digitally controlled pulse deposition system can be found in our previous papers [35, 37]. Briefly, a high power pulse (pulse width: 2 μs; repeatable rate: 1–10 Hz; pulse energy: 5 J) CO_2 laser, focused with a 30 cm focal length of ZnSe lens, was incident at 45° onto a rotating (angular speed of circa was 150 rpm) pyrolytic hexagonal boron nitride (BN) target (99.99% purity, *B*/*N* ratio ~1.05, density ~1.94 g cc^{-1}) in a vacuum chamber. The laser beam focus spot on the surface of the target was about 2 mm in diameter, producing a power density in the order of 10^8 W cm^{-2} per pulse. Si wafers with a buffer layer of BN a few nanometers thick were used as substrates and positioned 4 cm away from the plasma source. The substrate temperature was controlled at around 450–500 °C during the entire 15 min of BN deposition. This procedure yielded boron nitride samples with a thickness up to 3 μm. Before deposition, a 5 nm flat BN buffer layer was deposited over the Si substrate in order to ensure high quality interface properties and protect the 2D BNNSs from atom diffusion at high temperatures.

2.2. Characterization

We have previously published several detailed structural analysis of BNNS films obtained by the PLPD technique [21, 32, 35, 38]. From these referred investigations, it was found that PLPD produces BNNS films consisting of a large number of

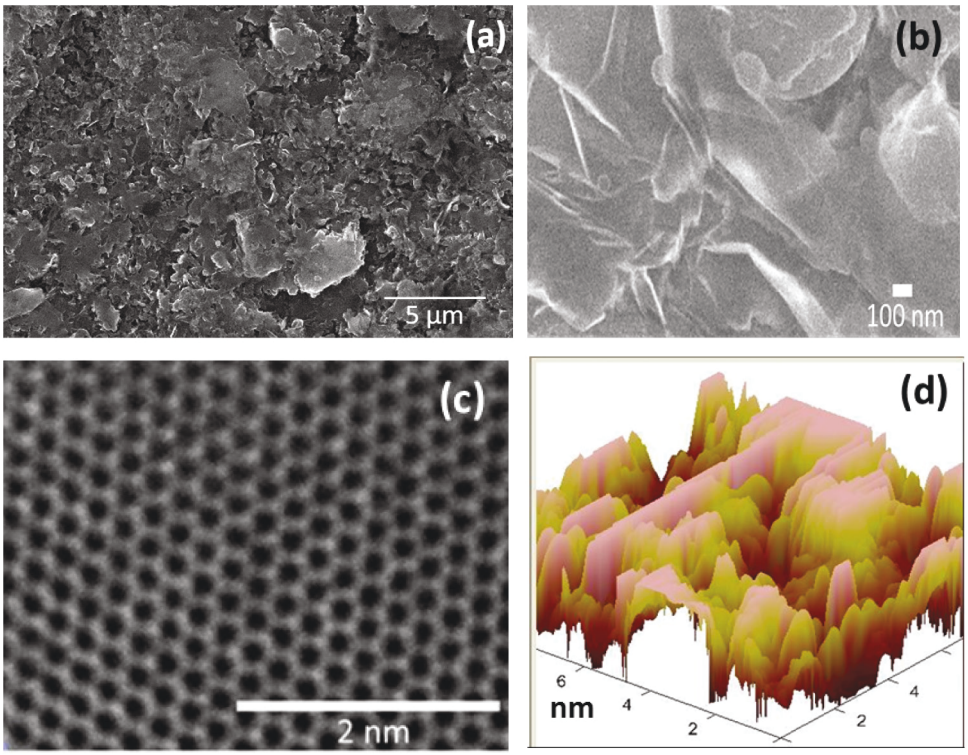

Figure 2. (a), (b) SEM images of BNNS sample prepared at 500 °C. (c) HRTEM and (d) AFM images of the surface of the BNNS sample.

randomly orientated nanosheets. Each BN nanosheet is composed of stacked *h*BN atomic layers with a wide distribution of *h*BN monolayers per nanosheet (see figure 1). A statistical analysis of high-resolution TEM images performed on thick BNNS films produced by PLPD [38] revealed that approximately 75% of BNNSs presented in the films were 4 to 5 nm in thickness or less and the remaining 25% larger than 8 nm. Additionally, BNNS packing within the film proved to form a variety of curved, elliptical and rippled nano structures [31]. In the current work, SEM, high-resolution transmission electron microscopy (HRTEM), atomic force microscopy (AFM), XRD and Raman scattering measurements were performed in order to investigate the structural quality of the individual BNNSs in the film and the film's surface properties.

Figures 2(a) and (b) show the SEM images of the BNNS films deposited on Si substrates at different magnifications. A rough, irregular and clustered surface type is observed revealing the disordered aspect of the films. This type of surface is consistent with what we would expect from films composed of BNNSs possessing a wide range of thicknesses, orientations and planar crystallite domain sizes. We can also observe that the film possesses a highly exposed surface area due to its irregular contour; a desirable trait in UV sensing materials. We have consistently found in previous works that purity of deposited BNNSs increases with temperature. As reported in [32], it was observed that 250 °C was the substrate critical temperature below which *h*BN was no longer formed. In this investigation and in our previous work [36], it was expected and determined that, contrary to the production of thin (nano range) BNNSs films, in order to produce thick films (micro range) of 'packed' BNNSs, substrate had to be kept within 400–500 °C. The HRTEM image of a single BN layer synthesized at 500 °C, shown in figure 2(c), illustrates the typical honeycomb arrangement of BN confirming that a high purity *h*BN sample was obtained.

In order to confirm the range of spatial orientations of the BNNSs relative to the substrate, AFM measurements were performed on the sample and the results are presented in figure 2(d). As observed in the figure, numerous planar structures representing individual BNNSs are present in the film having a wide range of possible orientations including vertical alignment.

The quality of the BNNS within the synthesized sample was further investigated by performing XRD and Raman measurements. XRD data in figure 3(a) reveals a single sharp peak characteristic of *h*BN's interlayer period, positioned at $2\theta = 26.66°$, which is 0.34° lower than the known XRD peak position of bulk *h*BN. We have reported on similar down shift of BNNSs XRD peak before [32] and has been attributed to the fact that the distance between the atomic layers of *h*BN in the nanosheets is larger than the reported interlayer spacing for the bulk material. The increased interlayer distance in BNNSs is known to be a contributing factor in band gap width depression [2]. Based on the interlayer distance determined by the XRD data from figure 3(a) and the BNNS thickness distribution described at the beginning of this section, 75% of BNNSs presented in the film have between 3 and 15 monolayers of *h*BN.

Figure 3(b) shows the BNNS film Raman spectrum. The *h*BN in-plane Raman active E_{2g} mode is clearly visible in figure 3(b). The intense and narrow peak (FWHM ~ 15 cm^{-1}) confirms that high quality and purity *h*BN nanosheets were obtained. The observed E_{2g} mode peak, positioned at 1356 cm^{-1}, appears redshifted compared to the bulk *h*BN

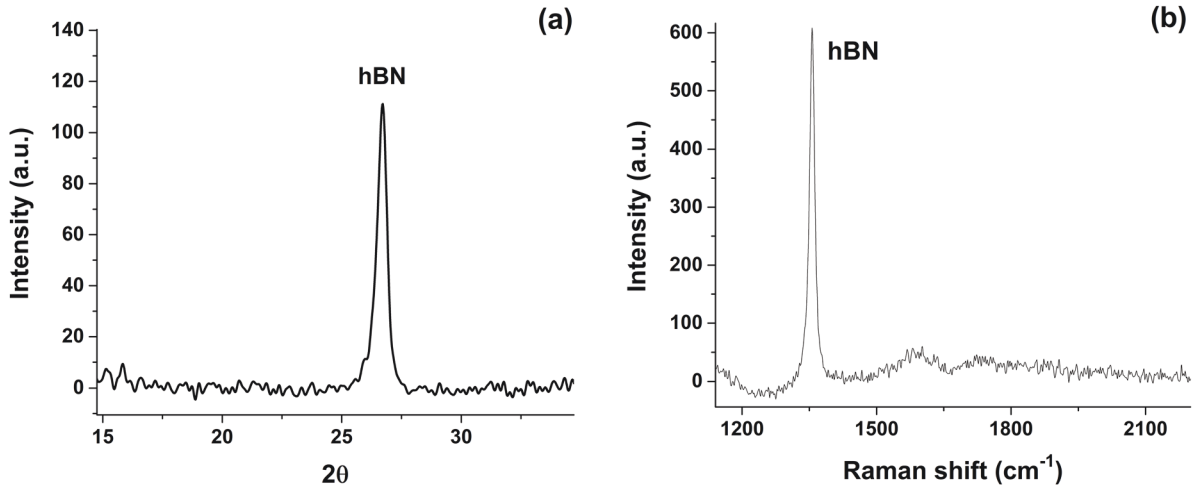

Figure 3. (a) XRD spectral intensity and (b) Raman spectral intensity of the BNNS film.

(1365 cm^{-1}). The increased interlayer distance observed from the XRD analysis strongly suggests that the interlayer energy landscape is significantly different in BNNS than in the bulk *h*BN. Such changes in this energy landscape will unavoidably produce alternative optimum stacking orders which could reflect in Raman spectrum. Such redshift in the Raman peak position has also been associated with a reduction bandgap width in BNNSs [31].

2.3. Device fabrication and experimental setup

Figure 4 shows the process flow for the fabrication of the prototypic photodetector and a schematic of the experimental set-up. Following the synthesis of the BNNS film on the *h*BN buffered silicon substrate, deposition of gold electrode pair via RF sputtering deposition technique was performed over the BNNSs film using a shadow mask rather than performing any lithography method. A detailed report can be found in our previous publications [39, 40]. The deposited Au electrodes had a thickness of 80 nm with a separation of 1 mm. The sensor's active area was 8 mm^2.

The schematic shown in figure 4, also includes a representation of the experimental setup utilized to characterize and test the UV sensing performance of the fabricated device. The prototype was serially connected to a precise resistor R_p and a step voltage power supply V_o. An electrical meter V was used to measure voltage variations across R_p during the characterization of the fabricated detector. A thermocouple and tungsten filament were used to control the operating temperature. The Tungsten filament heated the substrate from below hence heating occurs through the substrate. The entire system was controlled with a *LabVIEW* program.

With the setup described in figure 4, the dark current–voltage curves at different temperatures were obtained with less than 5% in measurement error. Following the dark current characterization of the prototype, the described prototype testing system was applied for photocurrent (I_{ph}) measurements. Different pen-ray UV lamps, emitting at 254 nm, 302 nm and 365 nm wavelengths, with varying intensities were used at this stage in order to fully characterize the photodetector's performance at different operating temperatures.

The photon-induced electrical current I_{ph} observed when the sensing material is exposed to UV radiation, is generated by incident photons that excite electrons from the valence to conduction band and some carriers are collected at the electrodes.

The induced photocurrent in the system is given by

$$I_{ph} = Gq\eta A\phi \tag{1}$$

where G is the photoconductive gain, η is the quantum efficiency, q is the electronic charge, A is the device area exposed to incident radiation, and ϕ is the incident flux [41]. In equation (1), the photoconductive gain G and the quantum efficiency η are the material dependent parameters determining any measured photocurrent. For an ideal photodetector, G is considered to be equal to unity, although several reports have discussed the contribution of observed photoconductive gain in photodetectors based on MSM architectures [42]. The responsivity of an ideal photodetector can be expressed as:

$$\mathrm{RES} = \frac{q\lambda}{hc}\eta \tag{2}$$

where q is the electron charge, λ the wavelength of the incident light, h is Planck's constant, c the speed of light and η is the quantum efficiency.

3. Results and discussion

Figure 5 shows the typical dark current of the fabricated prototype as a function of the applied bias voltage at different temperatures. A nonlinear *I–V* curve can be observed under dark condition indicating that a good double-Schottky contact behavior was formed between the metal electrode and the *h*BN film. At an applied voltage of 2 V, the measured current is 0.042 mA at room temperature and 0.122 mA at 150 °C. Dark current in Schottky devices is thermally activated with energy determined by the Schottky barrier height. However, additional photoconductive gain mechanisms could be providing additional contributions as suggested by the large magnitude of dark current and the general superlinear *I–V* behavior for voltages greater than 1 V [42].

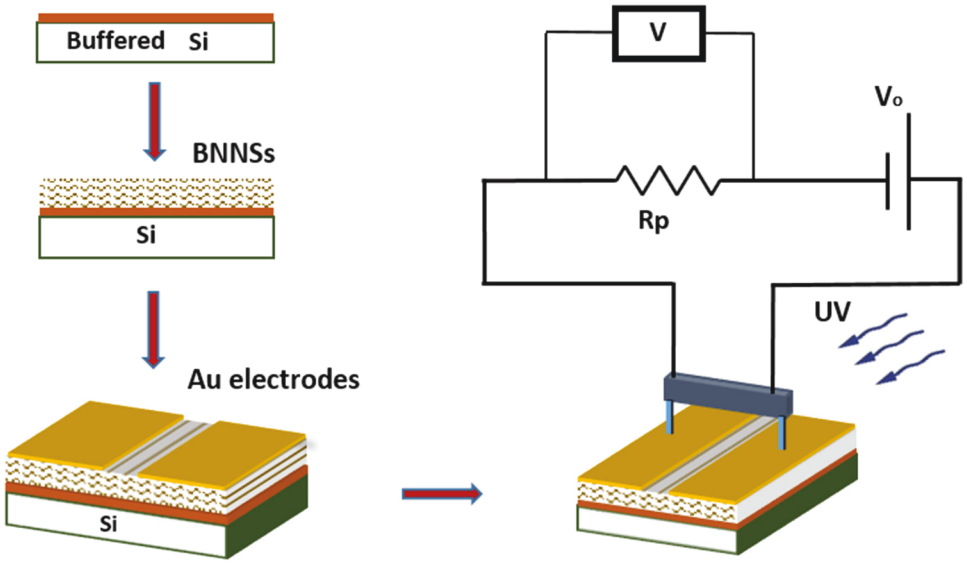

Figure 4. Prototype fabrication process applied to the BNNSs film and schematic of the experimental setup used in UV sensing tests of the fabricated prototype. Film thickness was 1.5 μm.

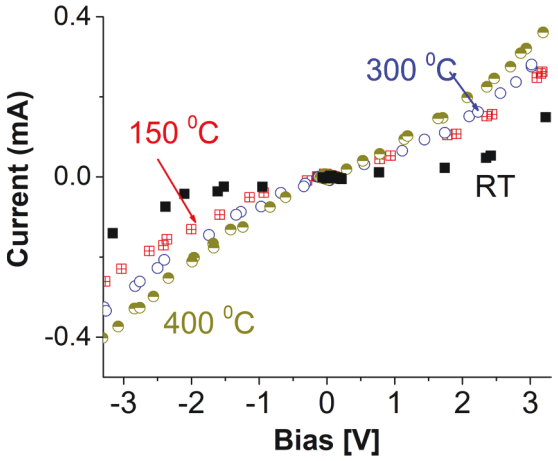

Figure 5. Measured dark current as a function of applied bias voltage at different temperatures.

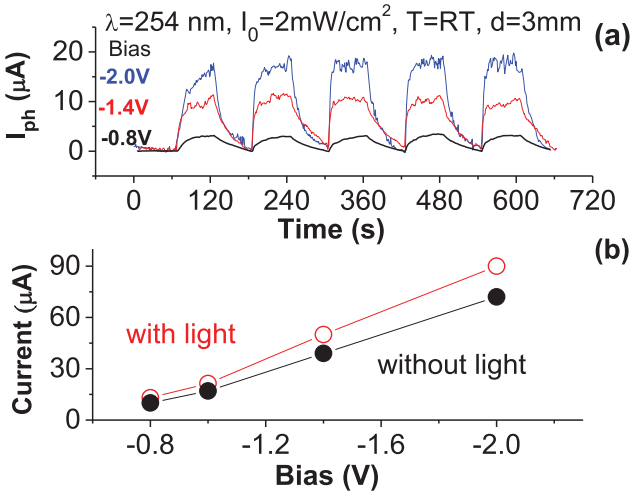

Figure 6. Bias effect on photocurrent: (a) photocurrent response when UV is cycled between on and off each 60 s and (b) the measured current as function of the applied bias with and without 254 nm UV light exposure.

On–Off cycles of 60 s each were performed on the fabricated device at different applied bias voltages in order to determine its effects on the measured photocurrent. The results are presented in figure 6. As seen in figures 6(a) and (b), when the BNNS prototype is exposed to a UV radiation source of 254 nm wavelength with power density $I_0 = 2$ mW cm^{-2} and placed 3 mm away from the sample, a photocurrent, I_{ph}, in the μA range is generated and becomes larger when the applied bias voltage is increased. Although I_{ph} increases with applied voltage, it is desirable to operate a UV photodetector at the lowest possible bias. Therefore, the UV sensing tests of the photodetector prototype were performed with an applied bias voltage of -1.4 V.

At a given applied bias operating voltage, the complete prototype sensor characterization includes photocurrent (I_{ph}), operating temperature range, responsivity (RES), response (t_{res}) and recovery (t_{rec}) times, stability and repeatability, as well as the cut-off frequency for determining the degree of visible-blindness.

3.1. Effects of incident UV light intensity

Light intensity at the surface of the detector was controlled by varying the distance d between the surface of the prototype and the center of the UV light source. In each case, a line source model was used to estimate the incident UV light intensity based on the distance since the UV lamps are one centimeter in length and 4 mm in diameter. Based on this model, when $d = 4$ mm the estimated UV incident light intensity reaching the surface of the photodetector was 1 mW cm^{-2}, and 0.13 mW cm^{-2} when the distance was 30 mm. As d increases, the intensity-distance relationships gradually approaches a point source model, therefore intensities calculated based on the line source model are likely to be slightly overestimated at the distances greater than about 14 mm. Therefore, it should be clarified that the RES values reported here represent a lower-limit to the actual value.

Figure 7 shows the photoresponse of the prototype to different intensities of UV light having a wavelength of 254 nm. The light source was cycled between on and off each 60 s. A well-defined photocurrent signal is observed from the fabricated detector exhibiting a stable baseline, good repeatability, and high signal-to-noise ratio. As expected, photocurrent decreases with distance from the light source due to the decrease in incident light intensity. The measured photocurrent ranged from 9.5 μA to 2 μA as the distance between the UV source and detector was varied from 4 mm to 44 mm. The responsivity of the detector, RES, defined as the photocurrent to incident light intensity ratio, is observed to have a maximum of 675 mA W^{-1} when $d = 30$ mm. Decreasing the light source distance below 30 mm increases I_{ph} disproportionately less than the increase in incident light intensity as saturation limit is approached. The responsivities (RES) obtained from the detector at the distances 4, 14, 30 and 44 mm in mA W^{-1} were 119, 385, 675 and 275, respectively. Real RES values are likely to be higher due to the previously mentioned overestimation of incident light intensities as d increases. This is a considerable improvement over our previous work on BNNSs and at par with other viable semiconductor based UV sensors like SiC at a much lower applied bias voltage, suggesting that this particular architecture of BNNSs has improved quantum efficiency [2, 16, 43–45]. Interestingly, application of equation (2) to the observed responsivities yields a quantum efficiency larger than 100%. This has been reported before and has been attributed to the contribution of photoconductive gain (G in equation (1)) [42].

As can be seen in figure 7, even when $d = 44$ mm (intensity equal or less than 0.09 mW cm^{-2}) where the measured photocurrent is minimum, the signal-to-noise ratio is still good and stable enough to obtain a distinguishable signal.

The sensor prototype exhibits a response time, t_{res}, in the order of several seconds (figure 7) when exposed to UV light of 254 nm wavelength. Additionally, t_{res} appears to improve upon cycling between on–off the UV light source. For example, when the sensor was 4 mm away from the light source, the response times for the first four cycles were 8, 6, 3 and 2 s, respectively. This pattern has been observed in the past by our group and others and has been attributed to humidity and environmental impurity effects which are reduced as cycling tests progress due to the increase in thermal energy provided by the cycling, although it is clear that many other factors besides humidity will have an influence on the response times [16, 46]. Interestingly, our previous work on BNNS and its UV sensing applications revealed that decreasing the number of *h*BN monolayers in BNNS to just a few atomic layers resulted in fast response times, less than 1 ms, compared to the samples composed of thicker BNNS. However, thick BNNS exhibited much higher photocurrent when exposed to UV radiation [2, 21]. It has been suggested that a fundamental trade-off between the photoconductive gain and the speed of a photodetector is unavoidable because a long minority carrier lifetime would result in photocurrent enhancement but increases the response time [39, 47, 48]. Compared to these previous BNNS structures tested, the present thick film of randomly orientated BNNSs appear to have minimized this trade-off

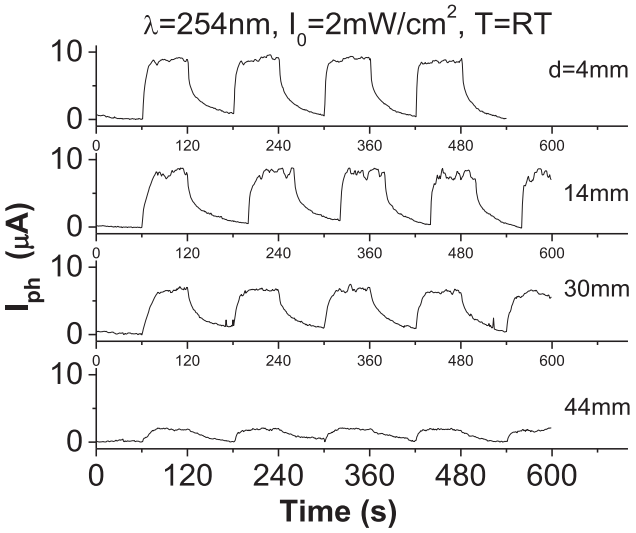

Figure 7. Measured photocurrent under 254 nm wavelength UV light cycling tests and varying distance d between the center of the light source and the prototype when biased at −1.4 V.

exhibiting a desirable balance between the sensitivity and the response time. The recovery time, on the other hand, appears to be considerably longer than the response time due to its intrinsic decay behavior towards the baseline. This recovery time behavior is very common but not well understood due to the complex, multifactor nature of these phenomena. It can be expected, however, that the real recovery time of the sensor is lower than it appears due to residual photoluminescence of the UV source at the beginning of an off cycle.

3.2. Effects of operating temperature

Additional UV cycling tests, presented in figure 8, were performed in order to investigate the effects of operating temperature on the UV sensing properties of the BNNS film.

A slight decrease in photocurrent, baseline quality and stability of the device under UV cycling test was observed as the operating temperature was increased. This is expected in UV sensing materials due to an increase in dark current and thermal noise. However, as seen in figure 8, the tested photodetector device performed extremely well at high operating temperatures. The obtained photocurrent was 7.6, 7.0 and 5.36 μA when operated at temperatures of 150, 300 and 400 °C respectively, which is a small decrease from the photocurrent obtained at room temperature. High signal-to-noise ratio and reproducibility were also observed even at temperatures as high as 400 °C and even with a relatively low bias of −1.4 V. This efficiency in operation and high photocurrent yield at such high temperatures is a vast performance improvement over any of our previous BNNS or SiC based photodetector prototypes [2, 16, 36] and in fact, besides single crystalline diamonds, few (if any) materials have demonstrated comparable UV sensing capabilities under such high operating temperatures. This makes BNNSs based deep UV photodetectors ideal candidates for many scientific and industrial applications where operation of sensors at high temperatures is required [2, 12, 16, 48].

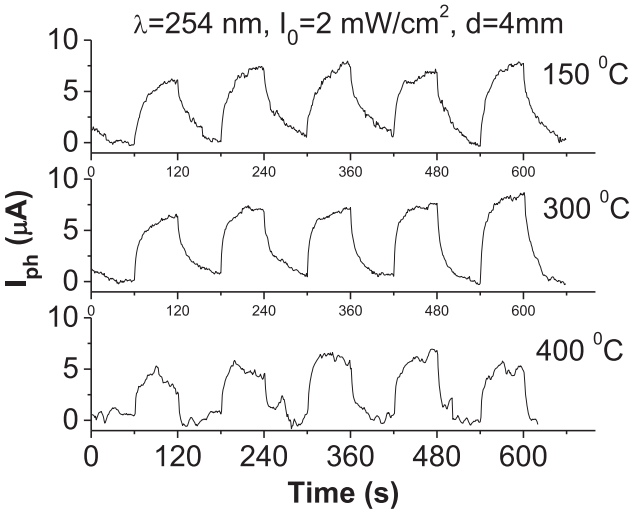

Figure 8. Temperature effect on UV photoresponse of the prototype under UV light of $\lambda = 254$ nm.

3.3. Cut-off wavelength

One of the main objectives for extending our work on applications of BNNSs as sensing material for UV photodetectors, has been to obtain a BNNS architecture with depressed energy band gap width in order to broaden the material's sensitivity range. The idea is to take advantage of nano-effects present in the BNNSs and other structurally derived properties in order to avoid the need of doping to expand the sensitivity since doping might compromise desirable features of *h*BN such as resistance to high temperatures. Previously conducted research by our group and others have shown that the nano-effects that emerge in BNNSs as the number of monolayers is significantly reduced, such as increased interlayer distance, can induce a reduction in band gap width compared to that of the bulk counterpart [2, 30, 31]. The XRD and Raman spectra of the currently investigated BNNS film, reveal similar nano-effect signatures capable of reducing the band gap width as the ones observed in these reports (see characterization section 2.2). However, such an effect has not been sufficient to create an effective sensor capable of sensing both UVB and UVC radiation.

Interestingly, as can be seen in figure 9(a), the fabricated prototype under investigation exhibits a clear response to UVB light of 300 nm in wavelength. With a maximum photocurrent of approximately 1.7 μA, the UV sensing cycling test in figure 9(a) exhibits a solid and stable baseline and response signal with high reproducibility. This result under 300 nm UV light represents an improvement in photocurrent of at least three orders of magnitude over any of our previous BNNSs based photodetectors [2, 36]. Moreover, at this wavelength the response and recovery times are significantly shorter, around 1 s or less, and consistent throughout the entire cycle. A similar effect was observed in our investigation of SiC, where response and recovery times were several orders less under UVB than that under UVC light [16]. It is possible that, as mentioned in section 3.1, the tradeoff between the I_{ph} and reaction times is a contributing factor in the observed differences in reaction times. However, the mechanism responsible for the response-recovery times of the detector is difficult to determine as it depends on many factors such as the nature of samples, charge carrier density, light wavelength, operating temperature, electrode arrangement, and humidity content, among many others.

The simplest explanation that addresses the prototype's sensibility to UVB light is the presence of impurities which contribute mid band gaps. For example, it was reported that BNNSs transitioned from an insulator to a semiconductor upon fluorination [49]. Additionally, theoretical calculations predict the presence of mid band gaps in *h*BN dopped with Si [50]. However, there are several indicators that suggest that the obtained electric measurements are due to the BNNSs and that the Si substrate most likely has only an indirect influence by providing preferential orientations of the deposited BNNSs. The main reason is the observed stability of operation when tested at high temperatures. Stability at high temperatures is difficult to obtain in doped-*h*BN due to the fact that doping changes many other properties of *h*BN besides conductivity. As mentioned in [50], doping BNNSs enhances chemical reactivity to numerous common gasses which would significantly alter our sample's UV performance as temperature is increased. This is probably why it is difficult to find any reports on the temperature dependence of electric properties of doped *h*BN. Also, doping causes large distortions in *h*BN sheets. Neither HRTEM nor XRD reflect the formation of any significant lattice deformations that would arise under Si doping. Therefore, if impurities were responsible for the apparent bandgap reduction, one would expect to observe a considerable change in the photocurrent and signal-to-noise ratio as temperature increases. But, as seen in figure 8, the prototype's performance is highly stable and exhibits little change in photocurrent when operated at 300 °C when compared to its performance at room temperature. It is worth mentioning that in our previous work on BNNSs deposited on AlN substrate an increase in photocurrent was observed as temperature increased. One possibility that could account for this difference in the photocurrents obtained at high temperatures in our previous and present work is that we do not have absolute control on the thickness of the BN buffer layer deposited on the substrate which forms via epitaxial growth. Another is that differences in substrate-buffer layer interactions in combination with differences in heat capacity and thermal conductivity of the substrates' material account for the observed difference in temperature dependence of the photocurrent. However, the exact reason for this observed difference is still unknown and deserves further research.

On the question of what could have possibly produce the observed transition of a known electrical insulator (bulk *h*BN) into a semiconductor, several publications have revealed doping-like effects as a result of the geometric properties of the edges of *h*BN nanostructures. For example, it was reported that *h*BN nonconducting nanotubes were observed to behave as a semiconductor once the nanotubes were 'unzipped' producing nanoribbons with exposed edges [51]. We suggest that that the observed semiconductor behavior and expansion of sensitivity to include UVB radiation in this case is the result

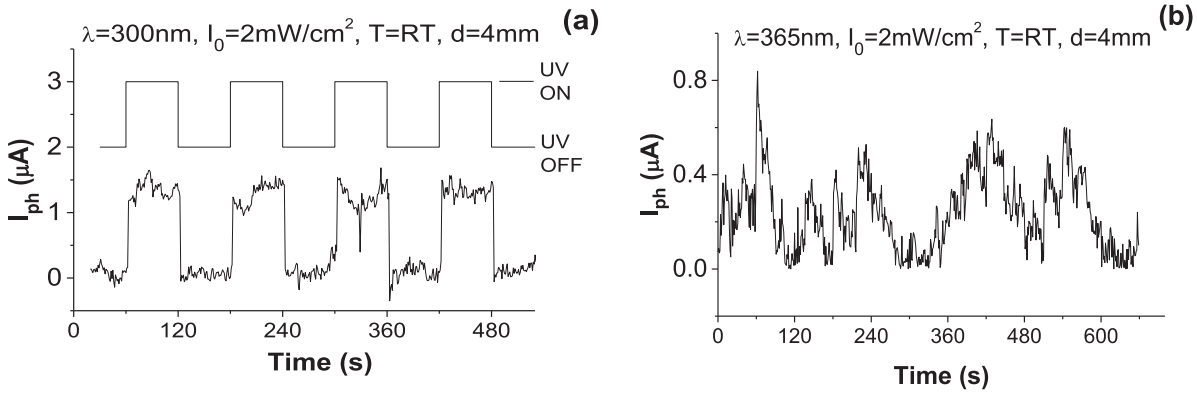

Figure 9. Photoresponse of the device at room temperature under (a) UV with $\lambda = 300$ nm and (b) $\lambda = 365$ nm.

of a collective behavior of the large number of thin randomly orientated and tightly packed BNNSs within the film.

This novel arrangement of numerous randomly orientated BNNSs tightly packed into a film would naturally result in a particular electronic structure which determines the material's UV sensing capabilities. However, determining the electronic structure in a BNNSs film is an extremely difficult task. Even in the case of bulk *h*BN, a lack of consensus within the field remains regarding its electronic structure due to the complex interplay between the interlayer positioning and the number of stacked monolayers interacting through weak van der Waals and electrostatic forces [52]. In the current case, the challenge in determining the electronic structure is compounded by additional factors, such as lattice defects and layer edge effects [51, 53–55]. For instance, Yu *et al* synthesized high-quality vertically aligned BNNS and tested their feasibility in UV applications [33]. In cathodoluminescence spectral measurements, the vertically aligned BNNS exhibited strong UV light emission, ranging from 200 to 400 nm wavelengths. They attributed as a major factor for such broadband UV light emission to the large amount of open and exposed edges of the BNNSs due to their vertical alignment. Reports on first-principles theoretical calculations have demonstrated that band gap of BN can be modulated by changing direction of applied electric field or by mechanical strain, effects which are likely to have an influence on the material under investigation due to the tight packing of randomly orientated BNNSs within the film [27, 56, 57]. Moreover, because of the intrinsic anisotropy of BNNSs, the random orientations of the BNNSs present in the film are a form of quenched disorder capable of imposing extremely hard to predict random field effects. The random field effects produced by quenched disorder has been known to significantly alter physical properties of nanocomposites [58]. Taking this into account and given the wide distribution of BNNS thicknesses in our current BNNS film it is likely that the ability of our fabricated prototype to detect light in the UVB region is the result of the superposition of the edge, mechanical strain, applied electric field directions and quenched disorder effects, all provided by the random orientations of the BNNSs.

Finally, figure 9(b) shows the result of the prototype when tested under near-visible UV light. The response is highly contaminated by noise, generating a useless signal, indicating that, while the sensitivity range of the material has been successfully broadened, the sensor remains blind to the visible range of the spectrum. Similar non-response was obtained from the detector when a visible 400 nm violet light emitting diode was used as a light source or from white fluorescent light.

4. Conclusion

The present work is an extension of our previous reports on the use of different architectures of BNNS as sensing material in UV sensing applications. One important common denominator has been the use of a simple, fast, cost-effective procedure based on the pulsed laser plasma deposition (PLPD) technique that is capable of synthesizing large amounts of high purity BNNSs. In this report, we successfully applied PLPD to create thick films composed of randomly orientated high purity BNNSs over a Si substrate. Characterization via SEM, HRTEM, AFM, XRD and Raman spectrum, and photocurrent measurements consistently suggested that a reduction in bandgap width of the material, compared to previous reports of BNNS, had occurred due to the unique internal structure of the *h*BN film. UV cycling tests were performed and revealed a well-defined photocurrent signal with desirable properties such as stable baseline, good repeatability, good responsivity and high signal-to-noise ratio for UV radiation in the UVB and UVC range while remaining visible blind. In conclusion, the BNNSs film demonstrated to be an ideal and unique candidate as a UV sensing material capable of sensing most UV light frequencies within the UVB and UVC range and possessing overall high quality performance over a broad operating temperature range like few other materials are capable of, while simultaneously being highly energy efficient (low applied bias) in its operation.

Acknowledgments

This work is supported by the Army Research Office/DoD grant (62826-RT-REP) and NSF-CREST grant (1736093). The authors extend their appreciation to the International Scientific Partnership Program (ISPP) at King Saud University for support of this research work through ISPP#0058. Manuel Rivera acknowledges NASA fellowship support through the NASA Grant NNX15AI11H.

ORCID iDs

Manuel Rivera https://orcid.org/0000-0003-1467-5503

References

[1] Chen H, Liu K, Hu L, Al-Ghamdi A A and Fang X 2015 *Mater. Today* **18** 493–502
[2] Aldalbahi A and Feng P 2015 *IEEE Trans. Electron Devices* **62** 1885–90
[3] Pace E and De Sio A 2010 *Mem. S.A.It. Suppl.* **14** 84–9
[4] Alenezi M R, Henley S J and Silva S R P 2015 *Sci. Rep.* **5** 8516
[5] Zhang J L, Wu G, Chen H Z and Wang M 2013 *Org. Electron.* **14** 255–9
[6] The International Commission on Non-Ionizing Radiation Protection 2004 *Health Phys.* **87** 171–86
[7] Whitehead R F, De Mora S J and Demers S 2000 *The Effects of UV Radiation in the Marine Environment* (Cambridge: Cambridge University Press) pp 1–34
[8] Mancebo S E and Wang S Q 2014 *Rev. Environ. Health* **29** 265–73
[9] Leckner B 1978 *Sol. Energy* **20** 143–50
[10] Lin C R, Wei D H, BenDao M K, Chen W E and Liu T Y 2014 *Int. J. Photoenergy* **2014** 492152
[11] Liao M, Sang L, Teraji T, Imura M, Alvarez J and Koide Y 2012 *Japan. J. Appl. Phys.* **51** 090115
[12] Tsai D-S, Lien W-C, Lien D-H, Chen K-M, Tsai M-L, Senesky D G, Yu Y-C, Pisano A P and He J-H 2013 *Sci. Rep.* **3** 2628
[13] Jiang H X and Lin J Y 2014 *Semicond. Sci. Technol.* **29** 084003
[14] Liu Z, Li F, Li S, Hu C, Wang W, Wang F, Lin F and Wang H 2015 *Sci Rep.* **5** 14420
[15] Xu X, Xu C and Hu J 2014 *J. Appl. Phys.* **116** 103105
[16] Aldalbahi A, Li E, Rivera M, Velazquez R, Altalhi T and Feng P 2016 *Sci. Rep.* **6** 23457
[17] Peng L, Hu L and Fang X 2013 *Adv. Mater.* **25** 5321–8
[18] Li L *et al* 2010 *Adv. Mater.* **22** 3161–5
[19] Fang X S *et al* 2009 *Adv. Mater.* **21** 2034–9
[20] Fang X S *et al* 2009 *Adv. Mater.* **21** 5016–21
[21] Sajjad M, Jadwisienczak W M and Feng P 2014 *Nanoscale* **6** 4577–82
[22] Zhang H Z, Phillips M R, Fitz Gerald J D, Yu J and Chen Y 2006 *Appl. Phys. Lett.* **88** 093117
[23] Oku T, Koi N and Suganuma K 2008 *J. Phys. Chem. Solids* **69** 1228–31
[24] Gao R, Yin L, Wang C, Qi Y, Lun N, Zhang L, Liu Y-X, Kang L and Wang X 2009 *J. Phys.Chem.* C **113** 15160–5
[25] Golberg D, Bando Y, Huang Y, Terao T, Mitome M, Tang C and Zhi C 2010 *ACS Nano* **4** 2979–93
[26] Lin Y and Connell J W 2012 *Nanoscale* **4** 6908–39
[27] Park C-H and Louie S G 2008 *Nano Lett.* **8** 2200–3
[28] Jin C, Lin F, Suenaga K and Iijima S 2009 *Phys. Rev. Lett.* **102** 195505
[29] Li L H and Chen Y 2016 *Adv. Funct. Mater.* **26** 2594–608
[30] Zhang Z, Guo W and Yakobson B I 2013 *Nanoscale* **5** 6381–7
[31] Feng P, Sajjad M, Li E Y, Zhang H, Chu J, Aldalbahi A and Morell G 2014 *Beilstein J. Nanotechnol.* **5** 1186–92
[32] Aldalbahi A, Zhou A F and Feng P 2015 *Sci. Rep.* **5** 16703
[33] Yu J, Qin L, Hao Y, Kuang S, Bai X, Chong Y-M, Zhang W and Wang E 2010 *ACS Nano* **4** 414–22
[34] Pakdel A, Zhi C, Bando Y and Golberg D 2012 *Mater. Today* **15** 256–65
[35] Sajjad M, Peng X Y, Chu J, Zhang H X and Feng P X 2013 *J. Mater. Res.* **28** 1747–52
[36] Rivera M, Velazquez R, Aldalbahi A, Zhou A F and Feng P 2017 *Sci. Rep.* **7** 42973
[37] Aldalbahi A, Zhou A F, Tan S and Feng P 2016 *Rev. Nanosci. Nanotechnol.* **5** 79–92
[38] Sajjad M, Ahmadi M, Guinel M J, Lin Y and Feng P 2013 *J. Mater. Sci.* **48** 2543–9
[39] Lee P, Feng X, Zhang G, Liu M and Lee S 1997 *Plasma Sources Sci. Technol.* **6** 343–8
[40] Lee S, Lee P, Zhang G, Feng X, Gribkov V, Liu M, Serban A and Wong T K S 1998 *IEEE Trans. Plasma Sci.* **26** 1119–26
[41] Razeghi M and Rogalski A 1996 *J. Appl. Phys.* **79** 7433–73
[42] Soares S F 1992 *Japan. J. Appl. Phys.* **31** 210–6
[43] Lees J E, Barnett A M, Bassford D J, Stevens R C and Horsfall A B 2011 *J. Instrum.* **6** C01032
[44] Liu H, Mcintosh D, Bai X, Pan H, Liu M, Campbell J C and Cha H Y 2008 *IEEE Photonics Technol. Lett.* **20** 1551–3
[45] Clark W R, Vaccaro K, Waters W D, Gribbon C L and Krejca B D 2014 *J. Lightwave Technol.* **32** 4780–4
[46] Lai C, Wang X, Zhao Y, Fong H and Zhu Z 2013 *RSC Adv.* **3** 6640–5
[47] Mukundan S, Roul B, Shetty A, Chandan G, Mohan L and Krupanidhi S B 2015 *AIP Adv.* **5** 127208
[48] Sang L, Liao M and Sumiya M 2013 *Sensors* **13** 10482–518
[49] Xue Y, Liu Q, He G, Xu K, Jiang L, Hu X and Hu J 2013 *Nanoscale Res. Lett.* **8** 49
[50] Liu Y J, Gao B, Xu D, Wang H M and Zhao J X 2014 *Phy. Lett.* A **378** 2989–94
[51] Zeng H, Zhi C, Zhang Z, Wei X, Wang X, Guo W, Bando Y and Golberg D 2010 *Nano Lett.* **10** 5049–55
[52] Gao W and Tkatchenko A 2015 *Phys. Rev. Lett.* **114** 96101
[53] Ooi N, Rairkar A, Lindsley L and Adams J B 2006 *J. Phys.: Condens. Matter* **18** 97–115
[54] Marom N, Bernstein J, Garel J, Tkatchenko A, Joselevich E, Kronik L and Hod O 2010 *Phys. Rev. Lett.* **105** 46801
[55] Kang J, Zhang L and Wei S-H 2016 *J. Phys. Chem. Lett.* **7** 597–602
[56] Zhang Z and Guo W 2008 *Phys. Rev.* B **77** 075403
[57] Qi J, Qian X, Qi L, Feng J, Shi D and Li J 2012 *Nano Lett.* **12** 1224–8
[58] Lopez I, Dolidze V and Aliev F 2010 *J. Non-Cryst. Solids* **356** 574–7